ELSEVIER

Earth and Planetary Science Letters 206 (2003) 509–528

EPSL

www.elsevier.com/locate/epsl

Low $^{3}He/^{4}He$ ratios in basalt glasses from the western Southwest Indian Ridge (10°-24°E)

Jennifer E. Georgen [a,*], Mark D. Kurz [b], Henry J.B. Dick [c], Jian Lin [c]

[a] *MIT–WHOI Joint Program in Oceanography, Woods Hole Oceanographic Institution, Woods Hole, MA 02543, USA*
[b] *Department of Marine Chemistry and Geochemistry, Woods Hole Oceanographic Institution, Woods Hole, MA 02543, USA*
[c] *Department of Geology and Geophysics, Woods Hole Oceanographic Institution, Woods Hole, MA 02543, USA*

Received 21 June 2002; received in revised form 5 November 2002; accepted 28 November 2002

Abstract

$^{3}He/^{4}He$ ratios and total helium concentrations have been measured in a suite of basalt glasses from the ultra-slow spreading (0.8 cm/yr half-rate) western Southwest Indian Ridge (SWIR). The study area is divided into two subregions, a supersegment between 9° and 16°E, where poorly defined ridge segments lie at a highly oblique angle to the regional spreading direction, and a supersegment between 16° and 24°E, where ridge segments are nearly orthogonal to the spreading direction. Although earlier geochemical studies suggested that the western oblique supersegment may be affected by the Bouvet plume more than 700 km to the west, there is no evidence for elevated $^{3}He/^{4}He$ in the region. In fact, $^{3}He/^{4}He$ throughout the entire study area ranges from 6.3 to 7.3 R_a, significantly below normal mid-ocean ridge basalt helium isotopic ratios of 8 ± 1 R_a. The preferred explanation for low $^{3}He/^{4}He$ ratios is recycled crustal or lithospheric material in the SWIR mantle source, although thorough evaluation of this explanation awaits additional geochemical data. ^{4}He concentrations for the oblique supersegment are generally lower than those for the orthogonal supersegment, which may reflect variable extents of magmatic degassing along the ridge. The low $^{3}He/^{4}He$ ratios are not attributable to radiogenic ingrowth following post-eruptive degassing, because ^{4}He concentrations are too high (>0.4 μccSTP/g). In addition to low ratios, $^{3}He/^{4}He$ measurements for the western SWIR are characterized by low variability, which contradicts predictions of an inverse relationship between spreading rate and helium isotope standard deviation. $^{3}He/^{4}He$ ratios for the orthogonal supersegment increase systematically from west to east, and are positively correlated with mantle Bouguer anomaly, a correlation which is opposite to that observed in other ridge environments. Overall, the range in $^{3}He/^{4}He$ isotopic values for the SWIR is significantly different from that measured along other ridges, suggesting that there may be systematic variability of $^{3}He/^{4}He$ ratios between ridge systems.

Keywords: Helium isotopes; Southwest Indian Ridge; Bouvet plume; geochemistry

* Corresponding author. Present address: Graduate School of Oceanography, University of Rhode Island, 232 Horn Laboratory, South Ferry Road, Narragansett, RI 02882, USA. Tel.: +1-401-874-6684; Fax: +1-401-874-6811.

E-mail addresses: jgeorgen@gsosun1.gso.uri.edu (J.E. Georgen), mkurz@whoi.edu (M.D. Kurz), hdick@whoi.edu (H.J.B. Dick), jlin@whoi.edu (J. Lin).

0012-821X/02/$ – see front matter © 2002 Elsevier Science B.V. All rights reserved.
doi:10.1016/S0012-821X(02)01106-8

1. Introduction

Along the global mid-ocean ridge system, areas affected by hotspots often have distinct geochemistry from 'normal' mid-ocean ridge basalt (MORB). Analyses of major element, rare earth element, and isotopic data for axial dredge samples can be merged with geophysical data such as bathymetry and gravity to delineate portions of ridge influenced by a nearby mantle plume [1–4]. Helium isotopic data are often a sensitive indicator of plume influence [5–7]. One assumption commonly made in interpreting noble gas data is that the hotspot source is relatively undegassed lower mantle. Under this assumption, high ^{3}He/^{4}He indicates plume-like upwelling, since the deep Earth is believed to be a source of primordial ^{3}He with a relatively low time-integrated (U+Th)/He ratio.

Values of ^{3}He/^{4}He for normal MORB (N-MORB) generally fall in the range of 8 ± 1, normalized to the atmospheric ratio of 1.384×10^{-6} (R_a) [9]. The assumption of a N-MORB value of 8 ± 1 R_a is based on along-axis studies (e.g. [5,10,11]) which omit significant ^{3}He/^{4}He variations near hotspots. More recent studies, incorporating data from a variety of geologic settings including ridges, back-arc basins, hotspot-influenced sections of ridge, and near-ridge seamounts, have questioned this value and suggest that the global mean ^{3}He/^{4}He ratio is 9.1 ± 3.5 R_a [12,13]. This estimate, however, suffers from numerous statistical effects, including the assumption that ^{3}He/^{4}He ratios are Gaussian-distributed and artifacts from spatial averaging of unevenly distributed data. This study makes use of MORB ratios of 8 ± 1 R_a as a benchmark [9]. However, the data presented here have implications for the definition of global average ^{3}He/^{4}He MORB values, particularly for the Southwest Indian Ridge (SWIR), because they are significantly below the putative 'normal' values.

Helium ratios around hotspots are often significantly different from those for N-MORB. For example, Hawaii has elevated ^{3}He/^{4}He, in the range of 8–32 R_a (e.g. [14–16]). In the vicinity of Iceland, ^{3}He/^{4}He increases from < 8 R_a south of the Gibbs Fracture Zone to ~ 15 R_a on the southern submarine portion of the Iceland plateau, to a high of 37 R_a on the island itself [17]. ^{3}He/^{4}He ratios in lavas from the Galapagos islands vary between 8.6 and 27 R_a (e.g. [10,18]). Moreover, Reunion Island helium measurements range from 11 to 14 R_a [19,20], and isotopic ratios for the SWIR near the Bouvet plume in the southern Atlantic Ocean reach 14.2 R_a [21].

There are also ocean islands and ridge segments with ^{3}He/^{4}He ratios lower than 8 R_a. Notably, most ^{3}He/^{4}He ratios along the Mid-Atlantic Ridge (MAR) near the Azores are as low as 7 R_a [5]. Graham et al. [22,23] found ratios along the southern MAR near Tristan da Cunha, Gough, and St. Helena to be uniformly less than 7 R_a. Possible explanations for low ^{3}He/^{4}He ratios include the addition of low He/(U+Th) material into the mantle source by recycling of subducted oceanic crust or delaminated continental lithosphere, and magma chamber or post-eruptive degassing followed by radiogenic ingrowth [5,24,25].

The goal of this investigation is to explore ^{3}He/^{4}He ratios along the western SWIR, between 10° and 24°E. This study area includes the slowest spreading rates for which ^{3}He/^{4}He ratios have yet been measured, as well as a section of ridge postulated to be affected by the Bouvet plume [26]. Surprisingly, for this ~ 800 km long portion of the SWIR, we report ^{3}He/^{4}He ratios that are both remarkably uniform and consistently below N-MORB values.

2. Geological and geochemical setting

2.1. Ridge geometry

The SWIR extends ~ 8000 km, from the Bouvet Triple Junction (BTJ) in the west to the Rodrigues Triple Junction in the east. Spreading rates along the SWIR are ultra-slow and relatively uniform, with half-rates ranging from 0.7 to 0.9 cm/yr. Two near-ridge hotspots, Bouvet and Marion, affect accretionary processes along the SWIR [27–30]. The Bouvet hotspot is located approximately 300 km east of the BTJ and ~ 50 km from the nearest spreading segment of the SWIR. Marion is approximately 250 km south of the

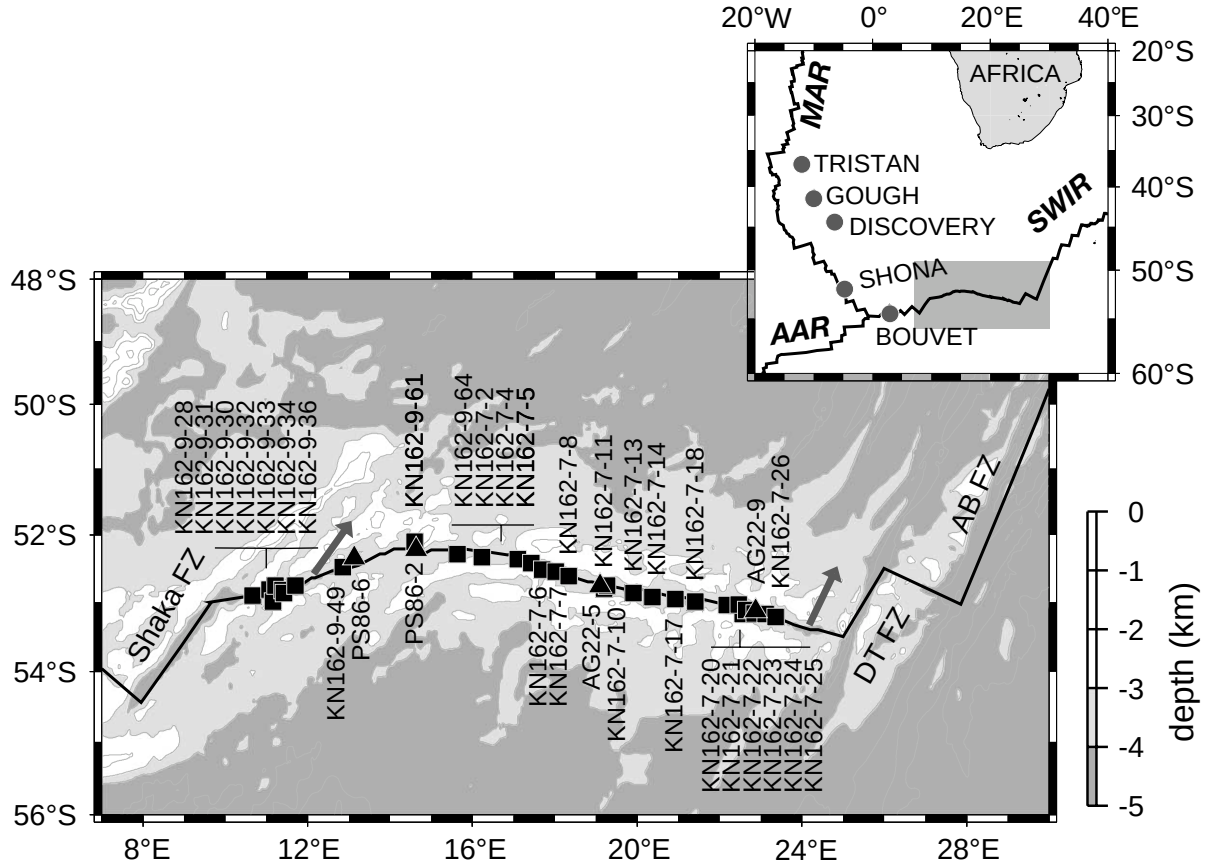

Fig. 1. Locations of the dredged samples analyzed in this study. Most samples are from *Knorr* cruise 162, legs 7 and 9 (KN162- designation, squares); samples with PS86- and AG22-prefixes (triangles) were obtained during Leg ANT IV/4 of the F.S. *Polarstern* (1986) and *Agulhas* Leg 22 (1981), respectively. Arrows indicate plate spreading direction [71-72]. The ridge axis between 9° and 16°E is referred to as the oblique supersegment because the ridge lies at a high angle to the regional spreading direction. In contrast, spreading is nearly perpendicular to the strike of the ridge between 16° and 25°E, referred to as the orthogonal supersegment. Ridge coordinates for the orthogonal supersegment are from Grindlay et al. [31]. Bathymetry data are extracted from the global predicted seafloor topography database [48]. The shallowest seafloor (shaded white) is <3 km deep; the contour interval is 1 km. DT FZ and AB FZ are the Du Toit and Andrew Bain fracture zones, respectively. Inset shows the regional setting of the study area, just to the east of the Bouvet Triple Junction at $\sim$0°E. The Bouvet Triple Junction joins the Southwest Indian Ridge (SWIR), American–Antarctic Ridge (AAR), and southern Mid-Atlantic Ridge (MAR). The locations of hotspots in the vicinity of the Bouvet Triple Junction are indicated with gray filled circles.

ridge axis in the central portion of the SWIR, to the east of the Andrew Bain Fracture Zone and well outside of the study area.

The western SWIR can be divided into three sections based on spreading geometry (Fig. 1). Between the BTJ and the Shaka Fracture Zone, well-defined short ridge segments, which are orthogonal to the regional spreading direction, are offset by relatively long-lived transform faults. In contrast, segmentation is poorly defined along the 400 km long section of ridge between 9° and 16°E. This portion of the SWIR lies at a high angle to the regional spreading direction, and consequently is referred to here as the oblique supersegment. Because of its obliquity, this SWIR section has an effective spreading rate, or spreading rate measured orthogonal to the local ridge trend, of only 0.42 cm/yr. This is the slowest rate along the accessible portion of the global ridge system (only the Arctic ridges are slower). Between 16° and

25°E, the SWIR is composed of a series of short (~42 km) segments separated by non-transform offsets [31]. Since ridge segments are only 10° from perpendicular to the regional spreading direction in this area, this portion of the SWIR will be referred to as the orthogonal supersegment. The orthogonal supersegment was the focus of a detailed geophysical survey by Grindlay et al. [31], while the recent R/V *Knorr* cruise 162 (Austral summer 2000–2001) surveyed bathymetry, magnetics, and gravity of the oblique supersegment and dredged >60 locations on both the oblique and orthogonal supersegments [32].

The BTJ is the intersection of the SWIR, American–Antarctic Ridge (AAR), and MAR. Over the past few million years, half-spreading rates for the AAR and MAR have been 0.9 and 1.4 cm/yr, respectively [33]. Spiess Seamount, a large volcanic edifice on the first SWIR segment to the east of the BTJ, may reflect recent reorganization of the triple junction and/or the present-day location of the Bouvet plume [29,33].

2.2. Geochemistry: BTJ vicinity and western SWIR

Values of ^{3}He/^{4}He in the immediate vicinity of the BTJ range from 6.5 to 14.2 R_a [21]. Along the SWIR, relatively high (9.98–12.9 R_a) values were obtained for four samples on the ridge segment closest to the Bouvet plume; a single measurement for Bouvet Island itself is 12.4 R_a [21]. Ratios for the segments flanking the Bouvet Ridge segment are relatively low (7.12–7.45 R_a); these ratios were attributed to ambient mantle ^{3}He/^{4}He values lower than the global average of 8 R_a [21]. Surprisingly, however, the highest measurements were obtained for the ridge segment between the Islas Orcadas and Shaka fracture zones, where a single dredge haul included rocks with ratios ranging from 7.41 to 14.9 R_a [21]. Along the eastern AAR, ^{3}He/^{4}He ratios are systematically higher near the BTJ (8.95–9.71 R_a), compared to lower values between 15° and 18°W (6.68–8.1 R_a) [21].

Four hotspots are located within 750 km of the southern MAR, Tristan, Gough, Discovery, and Shona (Fig. 1). As noted previously, Tristan and Gough are both low ^{3}He/^{4}He hotspots, with ratios <7 R_a [22,23]. However, both Shona and Discovery are characterized by well-defined axial ^{3}He/^{4}He highs, with maximum ^{3}He/^{4}He ratios of 14.7 and 14.2 R_a, respectively [7,21,25]. To the south of Shona, in the immediate vicinity of the BTJ, ^{3}He/^{4}He ratios of the MAR samples return to lower values of 7.11–7.66 R_a [21]. Note that these values are slightly lower than 8 R_a, the typical value for N-MORB.

Between the BTJ and 11°E along the SWIR, normal, transitional, and enriched MORB are juxtaposed with no clear gradient away from the Bouvet plume [34]. This geochemical variability is attributed to the ultra-slow spreading rate, which allows the persistence of small, localized plume-related heterogeneities without magma mixing or homogenization [26,34]. For the oblique supersegment, isotopic, major element, and trace element data are available for six dredge hauls collected prior to the KN162 cruises [26]. Dredged lavas are highly K-enriched, nepheline-normative alkali basalts and hawaiites with highly fractionated incompatible element ratios and enriched isotopic ratios. Le Roex et al. [26] explain these basalts as the products of extremely low percentage melting (<5%) of a veined mantle source. They postulate that the isotopically and trace-element-enriched veins result from lateral dispersion of the Bouvet plume more than 700 km away. A lack of published geochemical data for the orthogonal supersegment complicates evaluation of Bouvet contributions. However, several isotopic analyses of basalts from this region suggest that it is composed of isotopically depleted N-MORB [35]. Likewise, preliminary major element analysis of the same basalts used in this study suggests that the orthogonal supersegment erupts N-MORB [36].

2.3. Study motivation

This study documents variations in ^{3}He/^{4}He ratios along the western SWIR. Since these ^{3}He/^{4}He measurements correspond to the slowest spreading rates for which helium data are currently available, we first compare ^{3}He/^{4}He values from the oblique and orthogonal supersegments to

Table 1
Helium data for the western SWIR, oblique supersegment (10°–16°E)

Sample	Lat. (°S)	Long. (°E)	^{4}He conc. (μccSTP/g)	^{3}He/^{4}He (R/R_a)	±	Depth (m)	Method[a]
KN162-9-28-32	−52.90	10.67	0.0184	5.81	0.26	3803	1
			0.02096	3.76	0.16	3803	3
KN162-9-31-1	**−52.81**	**11.08**	**2.02**	**6.61**	**0.05**	**3074**	**1**
			0.01842	5.94	0.20	3074	3
KN162-9-30-12	**−52.99**	**11.16**	**2.97**	**6.49**	**0.04**	**3587**	**1**
			0.05126	6.11	0.10	3587	3
KN162-9-32-11	−52.75	11.22	0.00383	4.71	1.15	2720	1
			0.003793	5.94	1.28	2720	3
KN162-9-33-51	−52.82	11.39	0.0299	1.25	0.14	1462	1
			0.003740	0.77	1.35	1462	3
KN162-9-34-39	**−52.86**	**11.43**	**2.05**	**6.52**	**0.04**	**2126**	**1**
			0.07783	6.17	0.08	2126	3
KN162-9-36-27	−52.75	11.71	13.8	6.94	0.05	4017	1
KN162-9-49-13	**−52.48**	**12.86**	**1.55**	**6.80**	**0.04**	**4193**	**1**
			0.2274	6.70	0.07	4193	3
PS86-6-1	−52.35	13.13	0.0171	3.43	0.16	4000	2
PS86-6-2	−52.35	13.13	0.02819	3.21	0.07	4000	2
			0.00242	5.98	0.40	4000	1
			0.0227	3.05	0.05	4000	3
KN162-9-61-71	−52.10	14.60	0.01391	1.18	0.08	2282	1
			0.007611	0.35	0.11	2282	3
PS86-2-14	**−52.22**	**14.63**	**15.92**	**6.26**	**0.02**	**3200**	**2**
KN162-9-64-1	−52.29	15.64	0.006447	6.31	0.34	2947	1
			0.01321	6.40	0.21	2947	3

[a] 1 = Crushing in vacuo, 2 = melting in vacuo, 3 = melting of powder produced by crushing. Bold entries have ^{4}He concentrations greater than the threshold value of 0.4 μccSTP/g. Depths for PS- and AG-cruises are approximate.

measurements at faster spreading ridges. Second, we evaluate whether ^{3}He/^{4}He measurements differ systematically between the orthogonal and oblique supersegments, as a function of both proximity to the Bouvet hotspot and change in effective spreading rate. Third, we place the variability of ^{3}He/^{4}He along the western SWIR in a global context. Of particular interest is an evaluation of the hypothesis that ^{3}He/^{4}He variability for this ultra-slow spreading ridge should be high, given the linear relationship between reciprocal spreading rate and ^{3}He/^{4}He variance proposed by Allègre et al. [37].

3. Samples and analytical procedures

The samples described here primarily came from dredge sampling of the SWIR between 10° and 24°E during R/V *Knorr* legs 162-7 and 162-9 (Austral summer 2000–2001) [38]. Samples from Leg ANT IV/4 of F.S. *Polarstern* (1986) and the 1981 *Agulhas* Leg 22 cruise supplemented the *Knorr* dredges. KN162 recovered over 60 dredges along the SWIR axis, and the rocks varied in lithology and degree of alteration. The samples used in this investigation were selected for the availability of fresh basaltic glass. Vesicularities of the measured glasses range from $<1\%$ to 5%. In general, glasses from the oblique supersegment had more iron–manganese coatings, thinner glassy rims, and higher vesicularity than glasses from the orthogonal supersegment [38]. The locations of the analyzed basalts are indicated in Fig. 1 and Tables 1 and 2.

Fresh, completely vitreous glasses in the 0.5–2 mm size fraction were handpicked under magnification and cleaned ultrasonically in ethanol and acetone. The small size of these glass chips was necessary to avoid alteration. It is well known

Table 2
Helium data for the western SWIR, orthogonal supersegment (16°–24°E)

Sample	Lat. (°S)	Long. (°E)	^{4}He conc. (μccSTP/g)	^{3}He/^{4}He (R/R_a)	±	Depth (m)	Method[a]
KN162-7-2-1	**−52.33**	**16.23**	**0.6343**	**6.77**	**0.04**	**3855**	**1**
			0.4843	**6.58**	**0.03**	**3855**	**3**
KN162-7-4-31	**−52.36**	**17.11**	**2.972**	**6.67**	**0.03**	**3928**	**1**
			1.276	**6.55**	**0.04**	**3928**	**3**
KN162-7-5-1	**−52.42**	**17.43**	**1.106**	**6.64**	**0.04**	**3090**	1
			0.1906	6.52	0.03	3090	3
KN162-7-6-2	**−52.52**	**17.70**	**15.1**	**6.80**	**0.04**	**3582**	**1**
			10.58	**6.74**	**0.06**	**3582**	**2**
KN162-7-7-2	**−52.55**	**18.03**	**11.45**	**6.91**	**0.05**	**4001**	**1**
KN162-7-8-5	**−52.61**	**18.34**	**2.882**	**6.88**	**0.03**	**3702**	**1**
			3.679	**6.88**	**0.05**	**3702**	**3**
AG22-5-2	**−52.76**	**19.10**	**0.7269**	**6.97**	**0.03**	**3700**	**2**
AG22-5-7	**−52.76**	**19.10**	**3.541**	**7.03**	**0.06**	**3700**	**2**
AG22-5-18	**−52.76**	**19.10**	**0.717**	**6.87**	**0.03**	**3700**	**2**
AG22-5-14	−52.76	19.10	0.03521	6.67	0.10	3700	2
KN162-7-11-25	**−52.80**	**19.20**	**38.06**	**6.89**	**0.03**	**3886**	**1**
			7.449	**6.83**	**0.04**	**3886**	**3**
KN162-7-10-21	**−52.75**	**19.27**	**3.309**	**6.90**	**0.04**	**3165**	**1**
			2.787	**6.71**	**0.04**	**3165**	**3**
KN162-7-13-29	**−52.86**	**19.91**	**22.49**	**6.91**	**0.04**	**4071**	**1**
			7.144	**6.82**	**0.03**	**4071**	**3**
KN162-7-14-7	**−52.92**	**20.38**	**18.33**	**6.94**	**0.04**	**3450**	**1**
			3.820	**6.86**	**0.03**	**3450**	**3**
KN162-7-17-16	**−52.95**	**20.93**	**6.040**	**7.21**	**0.04**	**3874**	**1**
KN162-7-18-17	**−52.99**	**21.41**	**2.822**	**7.03**	**0.02**	**4507**	**1**
			10.06	**7.01**	**0.05**	**4507**	**3**
KN162-7-20-6	**−53.04**	**22.18**	**27.00**	**7.29**	**0.04**	**4246**	**1**
KN162-7-23-107	**−53.17**	**22.57**	**20.47**	**7.28**	**0.04**	**3658**	**1**
			1.626	**7.01**	**0.05**	**3658**	**3**
KN162-7-21-2	**−53.03**	**22.47**	**33.30**	**7.10**	**0.03**	**3787**	**1**
KN162-7-22-14	**−53.11**	**22.65**	**30.53**	**7.03**	**0.04**	**3875**	**1**
KN162-7-24-4	**−53.16**	**22.85**	**9.472**	**7.01**	**0.03**	**3290**	**1**
AG22-9-2	**−53.13**	**22.88**	**25.53**	**7.23**	**0.04**	**3800**	**2**
KN162-7-25-3	**−53.17**	**23.12**	**1.478**	**7.09**	**0.03**	**3995**	**1**
			12.53	**7.05**	**0.05**	**3995**	**3**
KN162-7-26-23	**−53.21**	**23.36**	**2.351**	**7.28**	**0.06**	**3325**	**1**

[a] 1 = Crushing in vacuo, 2 = melting in vacuo, 3 = melting of powder produced by crushing. Bold entries have ^{4}He concentrations greater than the threshold value of 0.4 μccSTP/g. Depths for PS- and AG-cruises are approximate.

that such small grain sizes may result in loss of gas in vesicles, which should be noted when comparing helium concentrations measured in this study to those obtained elsewhere. Helium measurements were generally performed by crushing in vacuo, although a number of samples were analyzed by melting. Crushing in vacuo selectively releases helium contained by vesicles, and is the preferred method here for two reasons. First, it minimizes post-eruptive radiogenic contributions from decay of Th and U, which reside in the solid matrix. Second, based on glass–vesicle equilibrium studies, a vesicularity of 1–5% corresponds to a vesicle/glass helium concentration ratio of 1 to 100 (e.g. [9]). Therefore, glass matrix ^{3}He/^{4}He ratios are more susceptible to change by radiogenic ingrowth both due to higher (U+Th) and because overall gas concentrations are lower. Concentrations for most samples were determined by both crushing and melting of the powder re-

maining from crushing, which then allowed estimation of total magmatic helium concentrations. All measurements were performed at Woods Hole Oceanographic Institution on a 90° sector mass spectrometer. Extraction lines for crushing and melting, mass spectrometry, and blank values are described elsewhere [16,39]. ^{4}He blanks during the course of these measurements were $\sim 6\times10^{-11}$ ccSTP.

Where both crushing and melting of glass chips were performed on the same sample (e.g. KN162-7-6-2), the isotopic composition determined by the two methods was identical within error, which demonstrates that the ^{3}He/^{4}He ratios obtained do not reflect any crushing-induced fractionation processes. This is confirmed by step-crushing experiments performed on several samples (KN162-7-11-25, KN162-7-18-17, and KN162-9-33-49). Helium released by both lighter crushing and more extensive crushing than the normal procedure yielded identical isotopic compositions in all cases.

Complete major element, rare earth element, and isotopic data sets are not yet available for the KN162 samples. Petrographic descriptions, as well as whole rock and glass analyses for the *Polarstern* samples, can be found in le Roex et al. [26]. Isotopic, major element, and trace element data for AG22-9-2 are described in Mahoney et al. [35].

4. Results and discussion

4.1. ^{4}He concentrations

The ^{4}He concentrations and ^{3}He/^{4}He ratios (R/R_a) are reported in Tables 1 (oblique supersegment) and 2 (orthogonal supersegment). Errors for the isotopic ratios are reported as 1σ; uncertainties in the ^{4}He concentrations are typically 1–2%. Total concentrations of ^{4}He (mostly calculated as the sum of crushing plus powder melting) vary widely, from 0.0076 μccSTP/g (sample KN162-9-32-11) to 45.5 μccSTP/g (sample KN162-7-11-25); this wide variation is not unusual and indicates the important influence of degassing processes on the measured helium contents

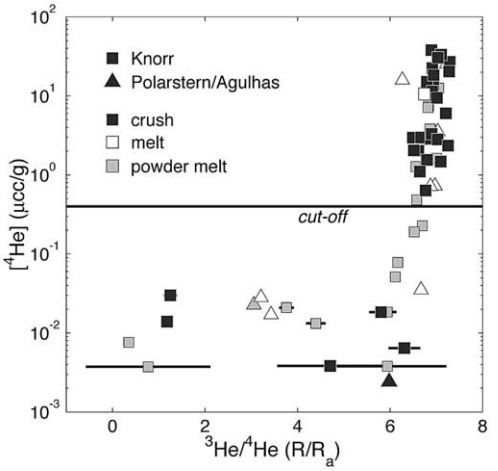

Fig. 2. Variation of ^{4}He concentration as a function of ^{3}He/^{4}He ratio. Only ^{3}He/^{4}He ratios for samples with ^{4}He concentrations above a cutoff of 0.4 μccSTP/g were considered representative of the mantle magmatic ratio, since low-^{4}He samples may have been affected by degassing and post-eruptive radiogenic ingrowth. For the remaining, high-^{4}He samples, ^{3}He/^{4}He ratios fall in the range of 6.3–7.3 R_a. The concentration threshold cutoff represented by a horizontal line at 0.4 μccSTP/g is explained in Fig. 5. All square symbols indicate glasses from KN162, while all triangle symbols represent samples from the PS86 or AG22 cruises. The shading of the symbol indicates the technique of helium measurement (black = crushing, unfilled = melting, gray = melting of the powder produced by crushing).

(Fig. 2). Wide variability of ^{4}He concentrations within a single dredge haul (e.g. AG22-5) reflects low glass availability and measurement of small glass chips ($\leq$0.5 mm) for some samples (e.g. AG22-5-14).

Fig. 3 shows that ^{4}He concentrations for samples from the oblique supersegment may generally be lower than those from the orthogonal supersegment. Lower concentrations for the oblique supersegment may reflect more extensive degassing during residence in magma chambers, in transit to the surface, and/or upon eruption on the seafloor. It is noteworthy that within samples from the orthogonal supersegment, there is an apparent relationship between longitude and total helium concentration, with significantly higher ^{4}He contents farther to the east (Fig. 3). ^{4}He contents range between 0.7 and 10.58 μccSTP/g in the western orthogonal supersegment samples (16.2–19.1°E) and between 6.0 and 45.5 μccSTP/g in the

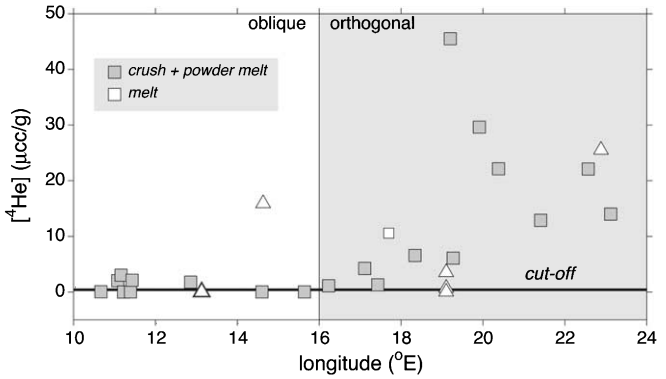

Fig. 3. Variation of total glass ^{4}He concentration as a function of longitude. Samples from the oblique supersegment and the western orthogonal supersegment have significantly lower total ^{4}He concentrations. This longitudinal difference may reflect variable degrees of magmatic degassing, or differences in mantle gas concentrations. The concentration threshold cutoff is represented by a horizontal line at 0.4 µccSTP/g as explained in Fig. 5. As in Fig. 2, squares represent samples from KN162, and triangles indicate samples from PS86 or AG22. Gas concentrations determined from the sum of melting and crushing are indicated with gray symbol shading, while those determined via melting of chips only are indicated with unfilled symbols.

east (19.2–23.4°E). Although shallower samples are often more degassed, possibly reflecting the effects of hydrostatic pressure on outgassing, there is not a strong relationship between ^{4}He concentration and dredge depth for the *Knorr* samples (Fig. 4).

^{3}He/^{4}He isotopic compositions of samples with extremely low gas contents may have been affected by degassing followed by post-eruptive radiogenic ingrowth or seawater interaction. To avoid overinterpretation of such data, this discussion focuses exclusively on samples with ^{4}He concentrations greater than 0.4 µccSTP/g. Over time scales of <1 Myr, it is unlikely that post-eruptive radiogenic ingrowth of ^{4}He by U+Th decay would affect the ^{3}He/^{4}He ratios of samples with concentrations higher than this. After 1 Myr of radiogenic ingrowth in a closed system, a sample with a ^{4}He concentration of 0.4 µccSTP/g and an initial ^{3}He/^{4}He ratio of 8 R_a would decrease by only 10% (Fig. 5), assuming a uranium concentration [U] of 0.6 ppm [21] and a Th/U ratio of 3 [40]. Although Th data are not yet available for the study area, the mean dredge-averaged [U] for the orthogonal supersegment is 0.11 ppm (range = 0.04–0.22 ppm), and for the oblique supersegment is 0.5 ppm (range = 0.06–1.60 ppm) (Standish et al., in preparation). The assumption of a relatively high [U] concentration of 0.6 ppm, therefore, yields an upper bound on ^{3}He/^{4}He ratio decrease due to radiogenic ingrowth.

A decrease in ^{3}He/^{4}He ratio of 10% is a significant threshold because the highest ^{3}He/^{4}He ratio among the samples was 7.29 R_a, approximately 10% below the N-MORB reference of 8 R_a. Moreover, $\sim$10 Myr would be required for the ^{3}He/^{4}He ratio for a sample with ^{4}He = 4 µccSTP/g to decrease by 10%. For ^{4}He = 40 µccSTP/g, ap-

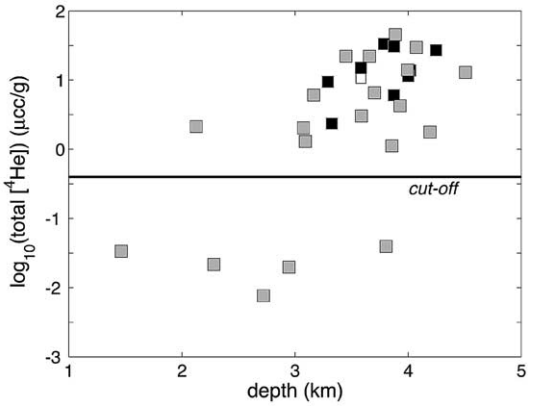

Fig. 4. Concentration of ^{4}He as a function of seafloor depth for the *Knorr* samples. ^{4}He concentrations for the *Polarstern* and *Agulhas* samples were not plotted because depths for these samples are poorly constrained. Symbols are as in Fig. 2. The concentration threshold cutoff represented by a horizontal line at 0.4 µccSTP/g is explained in Fig. 5.

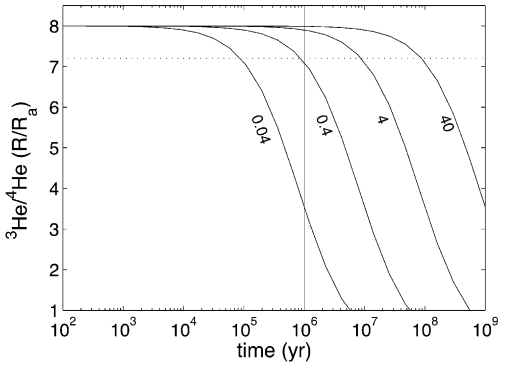

Fig. 5. Predicted time-dependent evolution of ^{3}He/^{4}He ratios resulting from post-eruptive radiogenic ingrowth of ^{4}He by decay of U+Th. Curves were calculated for four initial ^{4}He concentrations, 0.04, 0.4, 4, and 40 μccSTP/g, overlapping the concentration range observed in the SWIR sample suite. Assumptions include an initial ^{3}He/^{4}He ratio of 8 R_a, [U] of 0.6 ppm [21], and a Th/U ratio of 3 [40]. Dashed line indicates 10% reduction in initial ^{3}He/^{4}He ratio. This study interprets only samples with concentrations sufficiently high that post-eruptive radiogenic ingrowth does not lower their ^{3}He/^{4}He ratio below the 10% threshold for time scales <1 Myr. This concentration threshold corresponds to 0.4 μccSTP/g, and is indicated in Figs. 2–4.

proximately the highest concentration measured in this suite of basalts, this time scale is on the order of 100 Myr. In 1 Myr, the decrease in ^{3}He/^{4}He for ^{4}He = 40 μccSTP/g is smaller than analytical error. Therefore, a concentration cutoff of 0.4 μccSTP/g is very conservative both because the samples were dredged at the ridge axis and are most likely $\ll 1$ Myr in age, and also because these calculations assume fairly high Th+U concentrations.

4.2. Eruption ages

Helium isotope disequilibrium between vesicles and glass can be used to constrain the maximum eruption age of seafloor samples [21,41], a parameter that is of considerable interest in this ultraslow spreading environment. Because the (U+Th)/He method of dating is most successful for samples with low gas concentrations [41], we focus on glasses with melting-derived [^{4}He] below the concentration cutoff. We also calculate ages only for those samples for which ^{3}He/^{4}He$_{crush}$ differs from ^{3}He/^{4}He$_{powder\ melt}$ by more than 2σ. Additionally, we assume that [U] = 0.6 ppm [21], Th/U = 3 [40], helium was in equilibrium at eruption, and the only source of low ^{3}He/^{4}He ratios is radiogenic ingrowth. All samples that meet these requirements are from the oblique supersegment. As discussed above, the assumption of a uranium concentration of 0.6 ppm is close to the mean [U] of 0.5 ppm along the oblique supersegment, and falls within the measured range of 0.06–1.60 ppm (Standish et al., in preparation).

One set of model calculations assumes that initial isotopic compositions are equal to the ^{3}He/^{4}He ratios obtained by crushing. The resultant eruption ages range from 15 to 90 kyr (Table 3). In a second set of calculations, where the initial composition is set equal to the highest ^{3}He/^{4}He ratio obtained in the survey area (7.29 R_a), the

Table 3
Eruption ages

Sample	Crushing		Melting[a]		Age 1[b]	Age 2[b]
	^{4}He conc. (μccSTP/g)	^{3}He/^{4}He (R/R_a)	^{4}He conc. (μccSTP/g)	^{3}He/^{4}He (R/R_a)	(kyr)	(kyr)
KN162-9-28-32	0.0184	5.81	0.02096	3.76	60	82
KN162-9-31-1	2.02	6.61	0.01842	5.94	15	28
KN162-9-30-12	2.97	6.49	0.05126	6.11	24	67
KN162-9-34-39	2.05	6.52	0.07783	6.17	34	96
PS86-6-2	0.00242	5.98	0.0227	3.05	90	107
KN162-9-61-71	0.01391	1.18	0.007611	0.35	43	59

[a] Reported values correspond to melting of the powder produced by crushing.
[b] Age 1 was calculated by assuming that the initial isotopic composition was equal to the composition provided by crushing. Age 2 sets the initial composition to the highest ^{3}He/^{4}He ratio in the survey area, 7.29 R/R_a.

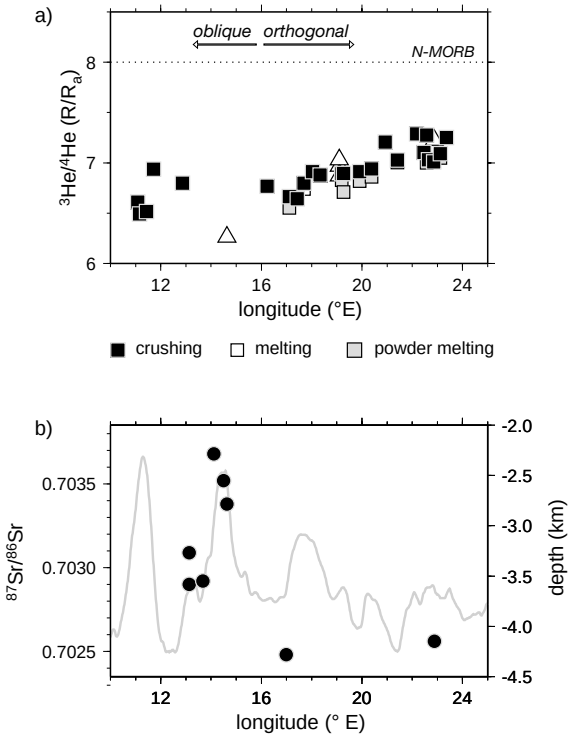

Fig. 6. (a) $^{3}He/^{4}He$ ratios along the SWIR between 10° and 24°E. Horizontal line at 8 R_a indicates average $^{3}He/^{4}He$ for normal mid-ocean ridge basalt (N-MORB). As in Fig. 2, symbol shape indicates cruise (squares = KN162, triangles = PS86 or AG22) and symbol color indicates helium analysis technique (black = crushing, unfilled = melting, gray = melting of the powder produced by crushing). (b) $^{87}Sr/^{86}Sr$ ratios along the oblique and orthogonal supersegments. Data are from le Roex et al. [26] and Mahoney et al. [35]. Gray line shows axial topography, extracted from the predicted topography database [48].

calculated eruption ages are slightly older, ranging from 28 to 107 kyr.

These calculations indicate that $^{3}He/^{4}He$ ratios for low-^{4}He samples can be significantly altered by post-eruptive radiogenic ingrowth on ~100 kyr time scales, and demonstrate the necessity of making measurements by crushing in vacuo and using a cutoff concentration. It should be clearly noted, however, that the complete suite of U and Th measurements is not yet available for these samples, and therefore these age calculations are only estimates. Also, in the absence of other rare gas isotopic data, it is difficult to rule out contributions by atmospheric contamination, as is suggested by near-atmospheric $^{3}He/^{4}He$ ratios in samples such as KN162-9-33-51 (1.25 R_a) and KN162-9-61-71 (1.18 R_a). Nevertheless, these calculated ages are geologically reasonable, and suggest that Th–U–He ages will be useful for MORB [21].

4.3. $^{3}He/^{4}He$ ratios

For samples with ^{4}He concentrations above 0.4 μccSTP/g, $^{3}He/^{4}He$ ratios vary between 6.3 and 7.3 R_a (Fig. 6a). These values are assumed to represent the mantle and are uniformly below the global average of 8 R_a for N-MORB, an observation that is discussed further below. $^{3}He/^{4}He$ ratios for the oblique supersegment show no systematic trend with longitude, though there are relatively few data points (Fig. 6a). In contrast, for the eastern portion of the study area, there is a trend of increasing $^{3}He/^{4}He$ ratios toward the Du Toit Fracture Zone (Fig. 7). Isotopic ratios for the samples east of 16°E are well described by a linear relationship between $^{3}He/^{4}He$ and longitude, with $r^2 = 0.71$. Over this region, $^{3}He/^{4}He$ ratios increase by approximately 0.8 R_a, or roughly 20 times the average 1σ measurement error.

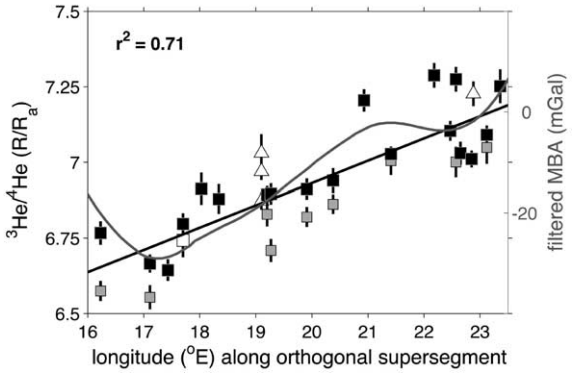

Fig. 7. $^{3}He/^{4}He$ ratios increase eastward along the orthogonal supersegment. Least-squares regression (black line) indicates that $^{3}He/^{4}He$ and longitude are correlated with $r^2 = 0.71$. There is also a correlation between long-wavelength mantle Bouguer anomaly (MBA, gray line) and $^{3}He/^{4}He$ ratios. The MBA profile was calculated by applying a 150 km cutoff lowpass filter to the MBA data in Grindlay et al. [31], sampled every 10 km. Symbols are the same as in Fig. 2.

As noted earlier, ^{4}He concentrations are generally lower in the western portion of the orthogonal supersegment than in the eastern portion. Interestingly, both long-wavelength mantle Bouguer anomaly (MBA, Fig. 7) and the geoid also increase from 16° to 24°E. Lower values of MBA indicate thickened crust, higher mantle temperatures, and/or lower crustal density [42,43]. A trend of eastward-increasing MBA along the orthogonal supersegment is generally consistent with the supersegment's position between the thermally warm BTJ region and the cool, long-offset Du Toit and Andrew Bain fracture zones [30]. However, a positive correlation between MBA and ^{3}He/^{4}He ratio is unusual in both hotspot-affected (e.g. Iceland) and non-hotspot-affected (e.g. Australian–Antarctic Discordance) settings, where the ^{3}He/^{4}He–MBA correlation is often negative [44,45]. Although a definitive explanation for this relationship is lacking, it is important to note that a prominent, roughly circular global geoid high, with a diameter of a few thousand kilometers, is centered at approximately the location of the Marion plume [46]. This geoid high indicates a deep-seated and spatially extensive planetary-scale density anomaly which could contribute to the gravity gradient observed for the orthogonal supersegment. In Iceland, the geoid and ^{3}He/^{4}He ratios decrease in concert away from the hotspot because both are controlled by the same plume. However, for the oblique and orthogonal supersegments, trends in the geoid may reflect long-wavelength convection processes outside the study area which are unrelated to local geochemical systematics. The positive ^{3}He/^{4}He–MBA correlation may therefore result from local ^{3}He/^{4}He variability superimposed on regional or planetary-scale gravity trends.

Although we do not have sufficient data to constrain the cause of the correlation between ^{4}He concentration and ^{3}He/^{4}He ratio along the orthogonal supersegment, we consider two possible explanations for the correlation. One plausible way of interpreting the low ^{4}He concentrations on the western side of the orthogonal supersegment is that basalts there have undergone more extensive degassing on the way to the surface. If that is the case, then the low glass helium concentrations are not source-related. Another plausible explanation for the low concentrations is that there was a recent mantle degassing event that lowered the ambient mantle helium concentrations, which could result in slightly lower ^{3}He/^{4}He ratios given sufficient time. For example, assuming 10% partial melting and typical U/Th ratios, the time required to significantly lower ^{3}He/^{4}He ratios would be on the order of 5–10 Myr. This would assume that the measured glass concentrations reflect actual mantle gas contents, unaffected by degassing in magma chambers or during eruption, or degree of partial melting. One mechanism that could result in mantle degassing is a past partial melting event. We speculate that the orthogonal supersegment's proximity to the BTJ may result in inheritance of mantle previously melted at the MAR and AAR.

4.4. ^{3}He/^{4}He variability and spreading rate

Because the SWIR samples were dredged from a portion of ridge with extremely slow spreading rate, it is important to compare their ^{3}He/^{4}He ratios to those obtained for samples from faster-spreading ridges. We compiled all available ^{3}He/^{4}He measurements for ultra-slow spreading SWIR, slow spreading MAR, and intermediate spreading Southeast Indian Ridge (SEIR) glasses from the RIDGE PETDB database [47], and supplemented this compilation with new analyses for the SEIR by Graham et al. [45]. Samples that occur within a plume-affected region were removed from the data set. We define plume-affected regions as areas with seafloor $> \sim 20\%$ shallower or deeper than a local baseline depth, following the methods of Ito and Lin [4] and using ridge topography profiles from [4,8,23,30,48–50]. We also eliminate measurements from the Australian–Antarctic Discordance (AAD) along the SEIR, an area with unusually cool mantle temperatures.

Examining similarly filtered data sets from the MAR, SWIR, Central Indian Ridge, Juan de Fuca Ridge, and East Pacific Rise, Allègre et al. [37] suggested a linear correlation between ^{3}He/^{4}He standard deviation and reciprocal spreading rate. Fig. 8 shows the correlation suggested by

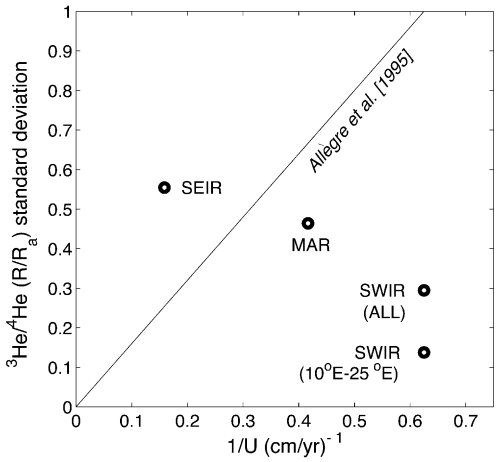

Fig. 8. Standard deviation of ^{3}He/^{4}He ratios measured on MORB glasses as a function of inverse spreading rate for the Mid-Atlantic Ridge (MAR), Southeast Indian Ridge (SEIR), and Southwest Indian Ridge (SWIR). To calculate ^{3}He/^{4}He variability, we first eliminated all samples lying within a plume-affected region. Plume-influenced regions were defined by axial depth anomalies following Ito and Lin [4]. Data from the Australian–Antarctic Discordance along the SEIR, a region with unusually cool mantle temperatures [65-66], were also eliminated. For each ridge, standard deviation was then calculated using all of the remaining samples after removing linear trends from the data. The relationship suggested by Allègre et al. [37], correlating high ^{3}He/^{4}He ratio standard deviation with slow spreading rate, is shown with a black line. The points for the SEIR ($n=85$), MAR ($n=93$), and SWIR (all, $n=44$), which reflect the improved global data set since 1995, do not strongly support such a correlation. Notably, the standard deviation for samples from 10° to 25°E along the SWIR is considerably lower than that for the MAR, SEIR, or total SWIR data sets.

Allègre et al. [37], with respect to the new SWIR data reported here. These data and the recent MAR and SEIR databases do not support a positive correlation between ^{3}He/^{4}He and spreading rate. However, it is clear from Fig. 8 that the samples from 10° to 24°E on the SWIR have significantly lower standard deviation than the MAR, SEIR, or full SWIR data sets. This relative uniformity in helium isotopic ratios is in strong contrast to the variability along the SWIR between the BTJ and 7°E, where ratios range from 7.12 to 14.9 R_a, as well as to the heterogeneity of other isotopic systems, such as ^{87}Sr/^{86}Sr ratios [26], discussed next.

4.5. Influence of the Bouvet plume on ^{3}He/^{4}He ratios

Based primarily on similarities between the Sr–Nd–Pb isotopic compositions of dredged glasses from 10° to 13°W and those from near Bouvet Island, le Roex et al. [26] suggested that the mantle beneath the oblique supersegment has been influenced by the Bouvet plume. Although the data are sparse, Fig. 6 shows that ^{87}Sr/^{86}Sr ratios of the oblique supersegment (0.7029–0.7036) are significantly higher than those of the orthogonal supersegment ($\sim$0.7025). Despite this and other geochemical evidence for influence of the Bouvet plume on the oblique supersegment [26], helium isotopes do not indicate that a deep-seated, relatively undegassed mantle plume is presently affecting accretionary processes along this portion of the SWIR. Over the oblique supersegment, ^{3}He/^{4}He ratios range from 6.26 to 6.94 R_a, significantly below values for N-MORB. Since Bouvet is a 'high ^{3}He/^{4}He' hotspot (with ratios up to 13 R_a), these values do not suggest mixing between a source with N-MORB ^{3}He/^{4}He ratios and a Bouvet plume end-member (Fig. 9). We explore three possible explanations for the apparent discrepancy between helium isotopes and other geochemical data. The first explanation involves spatial decoupling between helium and other isotopic systems in a broadly distributed Bouvet plume. The second explanation invokes distribution of discrete, enriched domains derived from a smaller Bouvet plume along the SWIR and AAR. The third, preferred explanation suggests that the low ^{3}He/^{4}He ratios are characteristic of a widely distributed, heterogeneous South Atlantic mantle source that does not necessarily require the involvement of the Bouvet plume.

4.5.1. Broad Bouvet plume

The first explanation posits that lateral dispersion of the Bouvet plume away from its vertically upwelling plume conduit at Bouvet Island (3°E) is broad. Absolute plate motion of the African and Antarctic plates would shear upwelling plume material to the east [51], similar to the case of the Galapagos plume [18]. For Galapagos, Kurz and Geist [18] postulate that helium is preferentially

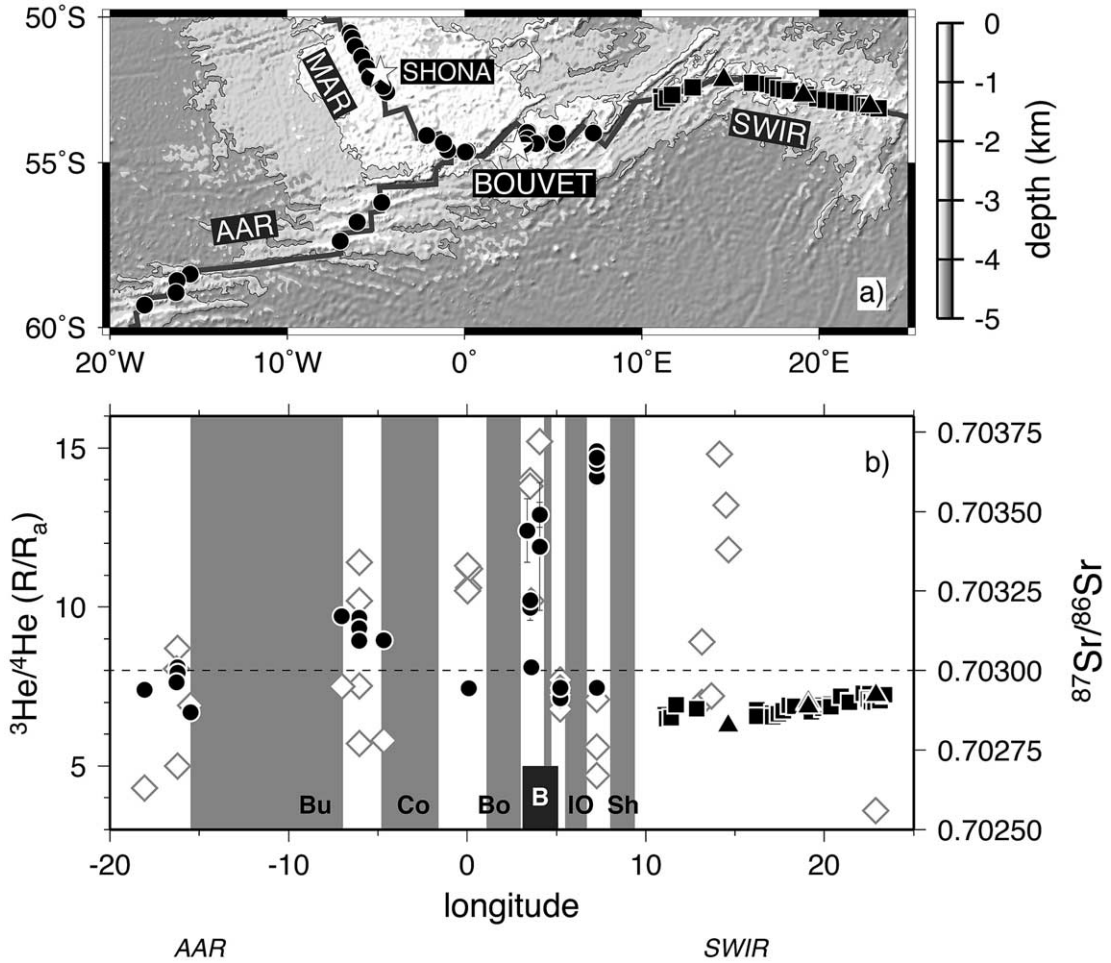

Fig. 9. (a) Map of predicted seafloor topography in the Bouvet Triple Junction region (data from [48]), showing the locations of $^3He/^4He$ measurements (squares are *Knorr* samples, triangles are *Polarstern*/*Agulhas* samples, and circles are from [21] or [7]). AAR = American–Antarctic Ridge, MAR = Mid-Atlantic Ridge, and SWIR = Southwest Indian Ridge. White stars give the positions of the Bouvet and Shona hotspots. Contour lines indicate 3 and 4 km depth, and an artificial illumination is imposed from the NW. (b) $^3He/^4He$ (filled symbols) and $^{87}Sr/^{86}Sr$ (diamonds) data along the AAR and SWIR. The names of selected fracture zones are labeled as Bu = Bullard FZ, Co = Conrad FZ, Bo = Bouvet FZ, IO = Islas Orcadas FZ, and Sh = Shaka FZ. Rectangle marked with a 'B' indicates the interpreted position of the Bouvet plume. Dashed line at 8 R/R_a indicates N-MORB $^3He/^4He$ reference level. Data are from le Roex et al. [26], Mahoney et al. [35], and Kurz et al. [21].

extracted from the vertically upwelling plume, resulting in $^3He/^4He$ values that are high at Fernandina, inferred to be directly over the plume conduit, and that decrease rapidly away from the plume center. In contrast, plume-like isotopic ratios of Sr, Nd, and Pb, elements assumed to be less incompatible than He, remain in the advected plume mantle farther away from the center of focused upwelling. By analogy, samples dredged far from the Bouvet conduit, but still within the range of Bouvet influence, could have low $^3He/^4He$ ratios but enrichments in other isotopic systems. In this way, the oblique supersegment could be influenced by Bouvet but lack high $^3He/^4He$ ratios.

Geophysical evidence strongly argues against the broad Bouvet plume hypothesis. For example, integrated analysis of gravity and bathymetry

data indicates that the Bouvet plume along-axis anomaly is strongly localized between the Bouvet and Islas Orcadas fracture zones, ~300 km from the oblique supersegment [30]. Moreover, although a broad thermal plume should be associated with thickened crust (e.g. [52]), crustal thickness for the oblique segment is likely to be significantly less than that of normal oceanic crust, as inferred from gravity analysis [53] and extensive recovery of peridotite over large regions of the seafloor [32]. Also, we have already noted that major element, trace element, and other isotopic data suggest that the Bouvet plume influence can be traced along the SWIR more than 700 km eastward from the inferred location of the upwelling plume [26]. Similar evidence exists for Bouvet plume influence along the AAR, to distances of as much as 1200 km away from the plume conduit [54]. As pointed out by le Roex et al. [54], it is unlikely that the geochemistry of approximately 2000 km of ridge is governed by direct lateral dispersion from such a diminutive plume as Bouvet. For comparison, the geochemical signature of Iceland, one of the largest plumes presently affecting the global mid-ocean ridge system [55] and significantly larger than Bouvet, is observed along approximately the same length of the MAR [56]. For these reasons, we discount invoking broad plume dispersal to explain the low $^{3}He/^{4}He$ values for the oblique supersegment.

4.5.2. *Dispersion of enriched mantle domains from Bouvet*

An alternative mechanism of Bouvet dispersion would involve upwelling plume material distributed throughout the ambient mantle in discrete enriched domains along the SWIR and AAR by long-wavelength asthenospheric flow [54]. As asthenospheric flow transports the enriched domain beneath a mid-ocean ridge, the domain melts to produce either E-, T-, or N-MORB, depending on the ratio of domain to ambient mantle that is melted. Unlike the broad plume hypothesis, this dispersion mechanism does not require an unduly large Bouvet plume flux. Le Roex et al. [26] suggest that the enriched domains are present to at least ~14.5°E. Because of limited geochemical data, it is unclear how much farther east these postulated enriched domains may extend, or whether or not there may be a gradient in domain volume from west to east. Application of geodynamic numerical modeling results of plume–ridge interactions [57,58] suggests that it is unlikely that domains from a low-flux Bouvet point source flowed more than 1500 km east to the orthogonal supersegment. Therefore, in view of the widespread nature of isotopic variability in the South Atlantic described in the following section, as compared to the more limited spatial distribution of Bouvet-related material, we next explore the notion that small-scale heterogeneity is characteristic of the South Atlantic mantle source, independent of the Bouvet plume.

4.5.3. *Nature of the South Atlantic mantle source*

In the immediate vicinity of Bouvet, low and high $^{3}He/^{4}He$ ratios are intermingled over short distance scales, in some cases within single dredges [21], suggesting melting of a heterogeneous mantle with at least two end-members, a high $^{3}He/^{4}He$ source and a low $^{3}He/^{4}He$ source. Interestingly, outside of the immediate influence of other hotspots like Shona and Discovery, low $^{3}He/^{4}He$ ratios are also observed throughout the South Atlantic, along the southern MAR, the AAR, and the SWIR [8,21,25]. The simplest explanation for the anomalous ratios observed in this investigation, therefore, may be that low $^{3}He/^{4}He$ ratios are characteristic of the entire ambient South Atlantic mantle, extending eastward to the Andrew Bain Fracture Zone complex along the SWIR. Unlike large plumes such as Iceland, the flux of the high $^{3}He/^{4}He$ Bouvet hotspot is insufficient to overprint the He systematics of this low $^{3}He/^{4}He$ mantle, and to create a coherent, long-wavelength trend of decreasing $^{3}He/^{4}He$ ratios away from the hotspot.

Compared to the relative uniformity of $^{3}He/^{4}He$ isotopes, systems such as Sr and Nd show striking variability throughout the study area (Figs. 6b and 9b). In dredges west of 16°E, $^{87}Sr/^{86}Sr$ ratios are variable and relatively high (0.70290–0.70368) compared to N-MORB [26]. Similarly, $^{143}Nd/^{144}Nd$ ratios are variable but generally range to low values (0.512837–0.513020) [26]. In contrast, east of 16°E, the few available

analyses suggest that $^{87}Sr/^{86}Sr$ ratios are low ($\sim$0.70250) while $^{143}Nd/^{144}Nd$ ratios are high ($\sim$0.51310) [35]. It would appear, therefore, that the required South Atlantic mantle source must be capable of generating a large range of Sr and Nd isotopic compositions at low degrees of melting. This variability may be explained by the presence of isotopically enriched mantle veins such as garnet pyroxenite. The relative uniformity of the isotopic composition of helium from 10° to 24°E is likely to reflect only the bulk composition of the mantle because of the rapid nature of He diffusion [59]. It is improbable that He isotopic disequilibrium between the veins and the ambient mantle could persist over mantle upwelling time scales. For example, using a diffusivity of 2×10^{-8} cm^2/s for clinopyroxene (at 1250°C; [59]), helium will diffuse almost 8 m in only 1 million years.

Pyroxenitic veins are widely distributed in small quantities ($<1\%$) in mantle xenoliths, alpine peridotites and ophiolites, and are believed to be common in the mantle [60]. Pyroxenitic veins may also have lower melting temperature than peridotite and could melt at greater pressures (e.g. [61]). Thus, where the absolute degree of melting is low, a small percentage of mantle vein material, relatively enriched in incompatible elements compared to the surrounding mantle peridotite, can potentially dominate the melt composition. In such a case, the isotopic systematics suggest two different melting scenarios for the oblique and orthogonal supersegments. In one scenario, the vein/ambient mantle ratio remains constant, but melt percentage increases, from west to east. Hotter mantle temperatures in the east could result from higher effective spreading rates along the orthogonal supersegment than the oblique supersegment [62,63]. Thus, in the west, Nd and Sr isotopic signatures would be dominated by melting of isotopically enriched mantle veins. In the east, however, at higher degrees of melting, melt compositions would be dominated by the isotopically depleted ambient mantle source, effectively masking the signal of the volumetrically smaller veins. In the second scenario, the degree of melting remains constant and relatively low throughout the study area, but the percentage or composition of the veins changes from west to east. However, this second scenario is inconsistent with the abundance of serpentinized peridotite and the near-absence of basaltic rocks over large regions of the seafloor along the oblique supersegment, which contrasts with the abundant basalt and scarce peridotite dredged along the orthogonal supersegment [32]. This contrast seems to require different extents of melting in the two supersegments.

As discussed in the next section, pyroxenite veins have also been proposed to explain low $^3He/^4He$ ratios observed in the Australian–Antarctic Discordance, a region of unusually low mantle temperature [45]. Although a veined mantle source could be consistent with the isotopic data currently available for the oblique and orthogonal supersegments, more thorough characterization of the South Atlantic mantle source awaits additional geochemical analyses of the basalts analyzed in this study, which will be published in a subsequent paper (Standish et al., in preparation). Accordingly, in the following section, we further speculate on the possible origin of the low $^3He/^4He$ signal.

4.6. Origin of low $^3He/^4He$ values

A salient characteristic of the oblique and orthogonal supersegments is $^3He/^4He$ ratios that are uniformly below the putative 'normal' MORB value. Fig. 10 shows $^3He/^4He$ frequency histograms for each of the ridges in Fig. 8. Compared to the MAR and SEIR, a large fraction of all non-plume-affected SWIR measurements are <7.5 R_a (Fig. 10b). Moreover, between 10° and 24°E, all existing measurements are <7.5 R_a. Although the previous section describes how a heterogeneous mantle source could relate to low $^3He/^4He$ ratios, several other potential causes of these low $^3He/^4He$ ratios are now evaluated.

4.6.1. Degassing

As discussed in an earlier section, degassing followed by post-eruptive radiogenic ingrowth of ^4He by decay of U+Th can lower time-integrated $^3He/^4He$ ratios. However, the use of a threshold ^4He concentration makes it unlikely that radiogenic ingrowth is sufficient to decrease SWIR

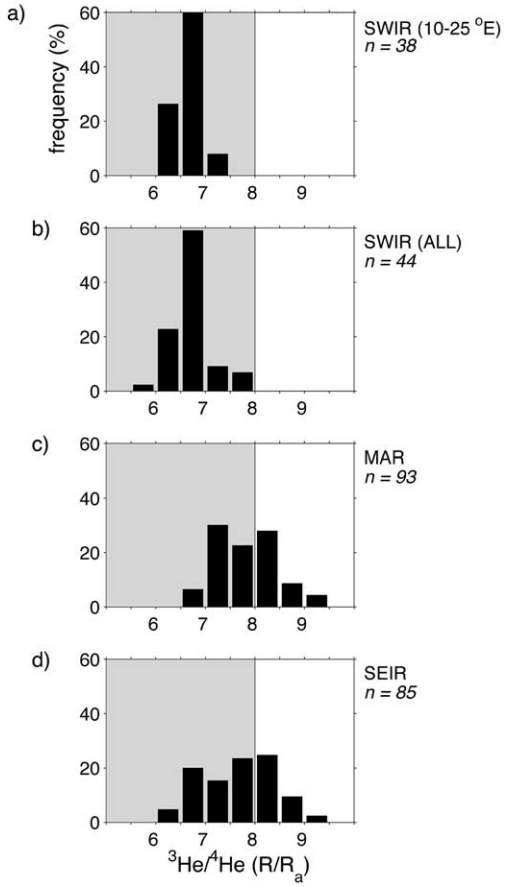

Fig. 10. Frequency histograms of $^3He/^4He$ ratios for non-plume-influenced MORB glasses from (a) the SWIR between 10° and 25°E, (b) the entire Southwest Indian Ridge, (c) the Mid-Atlantic Ridge, and (d) the Southeast Indian Ridge, excluding data from the Australian–Antarctic Discordance. Note that all samples available for 10–25°E SWIR have $^3He/^4He$ ratios below 7.5 R_a. As spreading rate increases, the peak in $^3He/^4He$ ratios appears to become less pronounced and may shift to higher values.

$^3He/^4He$ ratios by approximately 1–2 R_a, from 8 R_a to 6–7 R_a. Therefore, degassing alone does not seem to explain the low $^3He/^4He$ ratios.

4.6.2. Preferential melting of clinopyroxene

In a study of Juan de Fuca Ridge basalts, Lupton et al. [64] explain correlations between $^3He/^4He$ ratios, $Na_{8.0}$, and $Fe_{8.0}$ by invoking preferential melting of clinopyroxene. They point out that most U and Th in peridotite is located in clinopyroxene, and that clinopyroxene melting contributes relatively larger proportions to melts formed at lower temperatures. Therefore, they suggest that cooler, slower-spreading ridges should systematically have lower $^3He/^4He$ ratios than warmer, faster-spreading ridges. Although this explanation is consistent with low $^3He/^4He$ ratios at the ultra-slow spreading SWIR, rapid He diffusion makes it unlikely that mineral-scale isotopic heterogeneity can persist for characteristic time scales of >100 yr [59]. Thus, preferential melting of clinopyroxene at low mantle temperatures cannot explain low $^3He/^4He$ ratios.

4.6.3. Vertically stratified mantle

$^3He/^4He$ ratios as low as 6.2 R_a have been observed for basalts from the AAD [45]. Analysis of basalts [65] and numerical modeling work [66] suggest that mantle temperatures may be as much as 150°C lower in the AAD than along surrounding sections of the SEIR. Graham et al. [45] note a correlation between $^3He/^4He$ ratios and $Fe_{8.0}$, implying that lower $^3He/^4He$ ratios are associated with shallower depths of melting. Two possible explanations for this correlation include a vertically stratified mantle and melting of discrete heterogeneities [45]. The first explanation assumes that the upper mantle is vertically stratified, with relatively more degassed material with lower $^3He/^4He$ ratios overlying less degassed material. Since melting occurs at shallower depths for thermally cool ridges such as the western SWIR and eastern SEIR than for faster-spreading or warmer ridges, melts produced at cool ridges should have lower $^3He/^4He$ ratios. A good test of this hypothesis for the SWIR will come from $Fe_{8.0}$ variation along the orthogonal and oblique supersegments, data which are not yet available. Interestingly, the portion of the SWIR between the Melville Fracture Zone at 61°E and the Rodrigues Triple Junction at 70°E has the greatest axial depth along the entirety of the SWIR, suggesting anomalously cool mantle temperatures [67,68]. However, limited investigation of $^3He/^4He$ ratios from the eastern SWIR near the Rodrigues Triple Junction has yielded values of 7.68, 8.11, and 8.09 R_a [69], higher than values observed along the orthogonal and oblique supersegments and counter to the predictions of the vertically stratified

mantle model. Furthermore, three-dimensional thermal modeling calculations for passive plate separation predict that for depths within the melting region, axial temperature for the oblique supersegment is approximately 50–100°C lower than the orthogonal supersegment [62]. Therefore, if the vertically stratified mantle model applies, there should be a systematic difference between predicted, relatively low ^{3}He/^{4}He ratios along the oblique supersegment and predicted, relatively high ^{3}He/^{4}He ratios for the orthogonal supersegment. Although the predicted difference between oblique and orthogonal supersegment ^{3}He/^{4}He ratios may not be as great as the AAD ^{3}He/^{4}He anomaly because of the overall colder thermal regime of the SWIR, no such difference was observed.

4.6.4. Mantle heterogeneities

Preferential melting of discrete mantle heterogeneities with lower solidus temperature than surrounding material may also result in low ^{3}He/^{4}He ratios [45]. As described in an earlier section, for example, if crustal recycling veined the AAD MORB source with low-^{3}He/^{4}He garnet pyroxenite, then such veins would form a relatively large proportion of melt generated at cool ridges because they melt preferentially to mantle peridotite [45]. With increasing mantle temperature and depth of melting, mantle peridotite with higher ^{3}He/^{4}He would dilute garnet pyroxenite melts, resulting in MORB with higher ^{3}He/^{4}He ratios. In general, the most likely explanation for low ^{3}He/^{4}He ratios appears to be introduction of recycled crustal or oceanic lithospheric material (e.g. [5,22,24,70]), with relatively high (U+Th)/He ratios, into the source region for orthogonal and oblique supersegment MORB. It is possible that this recycled material is associated with the South Sandwich subduction zone, which is the closest subduction zone to the study area. It is important to note, however, that evaluation of this hypothesis requires geochemical data from the oblique and orthogonal supersegments that are not yet available.

Overall, the existence of low ^{3}He/^{4}He ratios over a long portion of the SWIR suggests that the average value of 8 ± 1 R_a for N-MORB may need to be referenced judiciously. It is possible that average MORB ^{3}He/^{4}He ratios vary between ridge systems. Currently, well-sampled ridges such as the slow-spreading MAR are over-represented in the global ^{3}He/^{4}He ratio database. The results of this study suggest that at least the ambient mantle beneath the ultra-slow spreading SWIR has ^{3}He/^{4}He ratios of 6.3–7.3 R_a, which are significantly lower than 8 ± 1 R_a. This conclusion is supported by glass data near the BTJ, which also indicate relatively low ^{3}He/^{4}He ratios [21].

5. Conclusions

The main results of this helium isotopic study along the western SWIR include the following:

1. ^{3}He/^{4}He isotopic ratios are uniformly lower than the putative MORB value (of 8 ± 1 R_a) along both the oblique supersegment (9° to 16°E) and the orthogonal supersegment (16° to 24°E) of the SWIR. ^{3}He/^{4}He ratios range from 6.3 to 7.3 R_a. These low ratios show that average values of ^{3}He/^{4}He for 'normal' MORB ratios must be used carefully, and may suggest that average ^{3}He/^{4}He ratios vary from ridge to ridge. The low ratios are not the result of post-eruptive radiogenic ingrowth processes. The preferred explanation is introduction of U+Th into the SWIR mantle source by recycling of crustal or lithospheric material, although detailed evaluation of this explanation awaits further geochemical data from the oblique and orthogonal supersegments. While the He data set alone cannot support or refute the existence of a veined mantle source for the SWIR, a veined mantle source is consistent with the different systematics of He, Nd, and Sr isotopes throughout the study area.
2. Despite prediction by earlier studies of an inverse relationship between ^{3}He/^{4}He variability and spreading rate, ^{3}He/^{4}He ratios between 10° and 24°E are relatively constant, with a standard deviation from the mean of approximately 0.1–0.2 R_a.
3. Although the total variation in ^{3}He/^{4}He ratios is relatively small, there is a systematic trend along the orthogonal supersegment with ^{3}He/

^{4}He ratios increasing from 6.6 to 7.3 R_a from west to east. Furthermore, ^{3}He/^{4}He is also significantly correlated with MBA along this trend. The glasses from the western end of the study area have significantly lower total ^{4}He concentrations than those from the east.

4. Despite a significant difference in ridge orientation between the orthogonal and oblique supersegments, there does not appear to be any systematic ^{3}He/^{4}He isotopic difference between the two ridge sections. Moreover, there is no evidence from ^{3}He/^{4}He data for influence of the high-^{3}He/^{4}He Bouvet plume on either supersegment.

Acknowledgements

We are grateful to the scientific party and crew of *Knorr* Leg 162, whose unparalleled dedication, perseverance, and resourcefulness made possible a very successful dredging program despite the most difficult of circumstances. We also acknowledge the tremendous assistance provided by Josh Curtice and Dempsey Lott, whose efforts and expertise in the laboratory made it possible to amass the SWIR data set in a remarkably short period of time. Jeff Standish is gratefully acknowledged for providing unpublished data, and for many helpful conversations. J.G. thanks the members of the WHOI Tectonics and Geodynamics discussion group, Bob Detrick, and Maria Zuber for their input and suggestions. The second and third authors contributed equally to this work. This work was supported by NSF Grants OCE-9811924 (J.L.), OCE-9907630 (H.J.B.D. and J.L.), and OCE-0002461 (M.K.). Woods Hole Oceanographic Institution contribution number 10694.***[BARD]***

References

[1] S.R. Hart, J.G. Schilling, J.L. Powell, Basalts from Iceland and along the Reykjanes Ridge: Strontium isotope geochemistry, Nature 246 (1973) 104–107.

[2] H.J.B. Dick, R.L. Fisher, W.B. Bryan, Mineralogic variability of the uppermost mantle along mid-ocean ridges, Earth Planet. Sci. Lett. 69 (1984) 88–106.

[3] J.-G. Schilling, Fluxes and excess temperatures of mantle plumes inferred from their interaction with migrating mid-ocean ridges, Nature 352 (1991) 397–403.

[4] G. Ito, J. Lin, Oceanic spreading center-hotspot interactions: Constraints from along-isochron bathymetric and gravity anomalies, Geology 23 (1995) 657–660.

[5] M.D. Kurz, W.J. Jenkins, J.G. Schilling, S.R. Hart, Helium isotopic variations in the mantle beneath the central North Atlantic Ocean, Earth Planet. Sci. Lett. 58 (1982) 1–14.

[6] R. Poreda, J.G. Schilling, H. Craig, Helium and hydrogen isotopes in ocean ridge basalts north and south of Iceland, Earth Planet. Sci. Lett. 78 (1985) 1–17.

[7] M. Moreira, T. Staudacher, P. Sarda, J.G. Schilling, C.J. Allègre, A primitive plume neon component in MORB: The Shona Ridge anomaly, South Atlantic (51-52 S), Earth Planet. Sci. Lett. 133 (1995) 367–377.

[8] D.W. Graham, K.T.M. Johnson, L.D. Prieve, J.E. Lupton, Hotspot-ridge interaction along the Southeast Indian Ridge near Amsterdam and St. Paul islands: helium isotope evidence, Earth Planet. Sci. Lett. 167 (1999) 297–310.

[9] M.D. Kurz, W.J. Jenkins, The distribution of helium in oceanic basalt glasses, Earth Planet. Sci. Lett. 53 (1981) 41–54.

[10] D.W. Graham, D.M. Christie, K.S. Harpp, J.E. Lupton, Mantle plume helium in submarine basalts from the Galapagos platform, Science 262 (1993) 2023–2026.

[11] R.J. Poreda, J.G. Schilling, Helium isotope ratios in Easter Microplate basalts, Earth Planet. Sci. Lett. 119 (1993) 319–329.

[12] D.L. Anderson, The statistics of helium isotopes along the global spreading ridge system and the central limit theorem, Geophys. Res. Lett. 27 (2000) 2401–2404.

[13] D.L. Anderson, A statistical test of the two reservoir model for helium isotopes, Earth Planet. Sci. Lett. 193 (2001) 77–82.

[14] M.D. Kurz, W.J. Jenkins, S.R. Hart, D.A. Clague, Helium isotopic variations in volcanic rocks from Loihi Seamount and the Island of Hawaii, Earth Planet. Sci. Lett. 66 (1983) 388–406.

[15] M.D. Kurz, D.P. Kammer, Isotopic evolution of Mauna Loa volcano, Earth Planet. Sci. Lett. 103 (1991) 257–269.

[16] M.D. Kurz, T.C. Kenna, J.C. Lassiter, D.J. DePaolo, Helium isotopic evolution of Mauna Kea volcano: first results from the 1-km drill core, J. Geophys. Res. 101 (1996) 11781–11791.

[17] D.R. Hilton, M.F. Thirwall, R.N. Taylor, B.J. Murton, A. Nichols, Controls on magmatic degassing along the Reykjanes Ridge with implications for the helium paradox, Earth Planet. Sci. Lett. 183 (2000) 43–50.

[18] M.D. Kurz, D. Geist, Dynamics of the Galapagos hotspot from helium isotope geochemistry, Geochim. Cosmochim. Acta 63 (1999) 4139–4156.

[19] D. Graham, J. Lupton, F. Albarede, M. Condomines, Extreme temporal homogeneity of helium isotopes at Piton la Fournaise, Reunion Island, Nature 347 (1990) 545–548.

[20] T. Staudacher, Ph. Sarda, C.J. Allègre, Noble gas systematics of Reunion Island, Indian Ocean, Chem. Geol. 89 (1990) 1–17.
[21] M.D. Kurz, A.P. le Roex, H.J.B. Dick, Isotope geochemistry of the oceanic mantle near the Bouvet triple junction, Geochim. Cosmochim. Acta 62 (1998) 841–852.
[22] D.W. Graham, S.E. Humphris, W.J. Jenkins, M.D. Kurz, Helium isotope geochemistry of some volcanic rocks from Saint Helena, Earth Planet. Sci. Lett. 110 (1992) 121–131.
[23] D.W. Graham, W.J. Jenkins, J.-G. Schilling, G. Thompson, M.D. Kurz, S.E. Humphris, Helium isotope geochemistry of mid-ocean ridge basalts from the South Atlantic, Earth Planet. Sci. Lett. 110 (1992) 133–147.
[24] S.R. Hart, A. Zindler, In search of a bulk-Earth composition, Chem. Geol. 57 (1986) 247–267.
[25] P. Sarda, M. Moreira, T. Staudacher, J.G. Schilling, C.J. Allègre, Rare gas systematics on the southernmost Mid-Atlantic Ridge: Constraints on the lower mantle and Dupal source, J. Geophys. Res. 105 (2000) 5973–5996.
[26] A.P. le Roex, H.J.B. Dick, R.T. Watkins, Petrogenesis of anomalous K-enriched MORB from the Southwest Indian Ridge: 11°53′E to 14°38′E, Contrib. Mineral. Petrol. 110 (1992) 253–268.
[27] R.A. Duncan, Hotspots in the southern oceans - an absolute frame of reference for motion of the Gondwana continents, Tectonophysics 74 (1981) 29–42.
[28] W.J. Morgan, Hotspot tracks and the early rifting of the Atlantic, Tectonophysics 94 (1982) 123–139.
[29] M. Ligi, E. Bonatti, G. Bortoluzzi, G. Carrara, P. Fabretti, D. Penitenti, D. Gilod, A.A. Peyve, S. Skolotnev, N. Turko, Death and transfiguration of a triple junction in the south Atlantic, Science 276 (1997) 243–245.
[30] J. Georgen, J. Lin, H.J.B. Dick, Evidence from gravity anomalies for interactions of the Marion and Bouvet hotspots with the Southwest Indian Ridge: Effects of transform offsets, Earth Planet. Sci. Lett. 187 (2001) 283–300.
[31] N.R. Grindlay, J. Madsen, C. Rommevaux-Jestin, J. Sclater, A different pattern of ridge segmentation and mantle Bouguer gravity anomalies along the ultra-slow spreading Southwest Indian Ridge (15°30′E to 25°E), Earth Planet. Sci. Lett. 161 (1998) 243–253.
[32] H.J.B. Dick, H. Schouten, J. Lin, Crustal accretion during extreme oblique spreading at an ultra-slow mid-ocean ridge, EOS Trans. AGU 82 (2001) S407.
[33] N.C. Mitchell, R.A. Livermore, Spiess Ridge: An axial high on the slow spreading Southwest Indian Ridge, J. Geophys. Res. 103 (1998) 15457–15471.
[34] A.P. le Roex, H.J.B. Dick, A.J. Erlank, A.M. Reid, F.A. Frey, S.R. Hart, Geochemistry, mineralogy and petrogenesis of lavas erupted along the Southwest Indian Ridge between the Bouvet Triple Junction and 11 degrees east, J. Petrol. 24 (1983) 267–318.
[35] J. Mahoney, A.P. le Roex, Z. Peng, R.L. Fisher, J.H. Natland, Southwestern limits of Indian Ocean ridge mantle and the origin of low $^{206}Pb/^{204}Pb$ mid-ocean ridge basalt: Isotope systematics of the central Southwest Indian Ridge (17°-50°E), J. Geophys. Res. 97 (1992) 19771–19790.
[36] J. Standish, H. Dick, A.P. le Roex, The influence of ridge geometry on mantle melting: Basalt geochemistry along the SWIR (9°-25°E), InterRidge South West Indian Ridge Workshop Abstracts Vol. 70, 2002.
[37] C.J. Allègre, M. Moreira, T. Staudacher, $^{4}He/^{3}He$ dispersion and mantle convection, Geophys. Res. Lett. 22 (1995) 2325–2328.
[38] H.J.B. Dick, J. Lin, H. Schouten, An investigation of the effects of ridge geometry on crustal accretion at ultra-slow spreading rates: The SW Indian Ridge from 9°-23.5°E, cruise report, R/V *Knorr* cruise 162, legs VII to IX (Dec. 9, 2000-Jan. 30, 2001), 2001.
[39] M.D. Kurz, J.J. Gurney, W.J. Jenkins, D.E. Lott, Helium isotopic variability from the Orapa Kimberlite, Earth Planet. Sci. Lett. 86 (1987) 57–68.
[40] K.L. Jochum, A.W. Hoffmann, E. Ito, H.M. Seufert, W.M. White, Potassium, uranium, and thorium in mid-ocean ridge basalt glasses and heat production, K/U, and K/Rb in the mantle, Nature 306 (1983) 431.
[41] D.W. Graham, W.J. Jenkins, M.D. Kurz, R. Batiza, Helium isotope disequilibrium and geochronology of glassy submarine basalts, Nature 326 (1987) 284–286.
[42] B.Y. Kuo, D.W. Forsyth, Gravity anomalies of the ridge-transform system in the South Atlantic between 31 and 34.5°S: Upwelling centers and variations in crustal thickness, Mar. Geophys. Res. 10 (1988) 205–232.
[43] J. Lin, G.M. Purdy, H. Schouten, J.-C. Sempere, C. Zervas, Evidence from gravity data for focused magmatic accretion along the Mid-Atlantic Ridge, Nature 344 (1990) 627–632.
[44] K. Breddam, M.D. Kurz, M. Storey, Mapping out the conduit of the Iceland mantle plume with helium isotopes, Earth Planet. Sci. Lett. 176 (2000) 45–55.
[45] D.W. Graham, J.E. Lupton, F.J. Spera, D.M. Christie, Upper-mantle dynamics revealed by helium isotope variations along the Southeast Indian Ridge, Nature 409 (2001) 701–703.
[46] F.G. Lemoine, S.C. Kenyon, J.K. Factor, R.G. Trimmer, N.K. Pavlis, D.S. Chinn, C.M. Cox, S.M. Klosko, S.B. Lutchke, M.H. Torrence, Y.M. Wang, R.G. Willianson, E.C. Pavlis, R.H. Rapp, T.R. Olson, The development of the Joint NASA GSFC and NIMI Geopotential Model EGM96, NASA Goddard Space Flight Center, Greenbelt, MD, 1998.
[47] C.H. Langmuir, Ryan, W.B.F., K. Lehnert, Y.J. Su, W. Jin, Petrological database of the ocean floor, http://petdb.ldeo.columbia.edu/petdb.
[48] W.H.F. Smith, D. Sandwell, Global sea floor topography from satellite altimetry and ship depth soundings, Science 277 (1997) 1956–1962.
[49] T.A. Minshull, N.J. Bruguier, J.M. Brozena, Ridge-plume interactions or mantle heterogeneity near Ascension Island?, Geology 26 (1998) 115–118.
[50] J. Douglass, J.G. Schilling, D. Fontignie, Plume-ridge interactions of the Discovery and Shona mantle plumes

with the southern Mid-Atlantic Ridge (40°-55°S), J. Geophys. Res. 104 (1999) 2941–2962.
[51] M.A. Richards, R.W. Griffiths, Thermal entrainment by deflected mantle plumes, Nature 342 (1989) 900–902.
[52] R.M. Allen, G. Nolet, W.J. Morgan, K. Vogfjord, B.H. Bergsson, P. Erlendsson, G.R. Foulger, S. Jakobsdottir, B.R. Julian, M. Pritchard, S. Ragnarsson, R. Stefansson, Crustal thickness across Iceland, EOS Trans. AGU 78 (1997) F500.
[53] J. Lin, H.J.B. Dick, H. Schouten, J. Georgen, Evidence for off-axis volcanic relicts of the Bouvet hotspot and its interaction with the Southwest Indian Ridge, EOS Trans. AGU 82 (2001) F1169.
[54] A.P. le Roex, H.J.B. Dick, A.M. Reid, F.A. Frey, A.J. Erlank, S.R. Hart, Petrology and geochemistry of basalts from the American-Antarctic Ridge, Southern Ocean: Implications for the westward influence of the Bouvet mantle plume, Contrib. Mineral. Petrol. 90 (1985) 367–380.
[55] N.H. Sleep, Hotspots and mantle plumes: Some phenomenology, J. Geophys. Res. 95 (1990) 6715–6736.
[56] G. Ito, J. Lin, C.W. Gable, Dynamics of mantle flow and melting at a ridge-centered hotspot: Iceland and the Mid-Atlantic Ridge, Earth Planet. Sci. Lett. 144 (1996) 53–74.
[57] N.M. Ribe, U.R. Christensen, The dynamics of plume-ridge interaction 2. Off-ridge plumes, J. Geophys. Res. 101 (1996) 16195–16204.
[58] G. Ito, J. Lin, C.W. Gable, Interaction of mantle plumes and migrating mid-ocean ridges: Implications for the Galapagos plume-ridge system, J. Geophys. Res. 102 (1997) 15403–15417.
[59] T.W. Trull, M.D. Kurz, Experimental measurements of ^{3}He and ^{4}He mobility in olivine and clinopyroxene at magmatic temperatures, Geochim. Cosmochim. Acta 57 (1993) 1313–1324.
[60] G.N. Hanson, Geochemical evolution of the suboceanic mantle, J. Geol. Soc. London 134 (1977) 1–19.
[61] M.M. Hirschmann, E.M. Stolper, A possible role for garnet pyroxenite in the origin of the 'garnet signature' in MORB, Contrib. Mineral. Petrol. 124 (1996) 185–208.
[62] J. Georgen, J. Lin, H.J.B. Dick, Models of mantle upwelling beneath the Southwest Indian Ridge: The effects of ridge-transform geometry on magma supply at an ultra-slow spreading ridge, EOS Trans. AGU 79 (1998) F854.
[63] H.J.B. Dick, J. Georgen, A.P. le Roex, J. Lin, J. Madsen, The influence of ridge geometry on mantle melting at an ultra-slow spreading ridge, EOS Trans. AGU 79 (1998) F919.
[64] J.E. Lupton, D.W. Graham, J.R. Delaney, H.P. Johnson, Helium isotope variations in Juan de Fuca Ridge basalts, Geophys. Res. Lett. 20 (1993) 1851–1854.
[65] E.M. Klein, C.H. Langmuir, H. Staudigal, Geochemistry of basalts from the South East Indian Ridge, 115°E-138°E, J. Geophys. Res. 96 (1991) 2089–2107.
[66] B.P. West, W.S.D. Wilcock, J.-C. Sempéré, L. Géli, Three-dimensional structure of asthenospheric flow beneath the Southeast Indian Ridge, J. Geophys. Res. 102 (1997) 7783–7802.
[67] C. Rommevaux-Jestin, C. Deplus, P. Patriat, Mantle Bouguer anomaly along an ultra-slow spreading ridge: Implications for accretionary processes and comparison with results from central Mid-Atlantic Ridge, Mar. Geophys. Res. 19 (1997) 481–503.
[68] M. Cannat, C. Rommevaux-Jestin, D. Sauter, C. Deplus, V. Mendel, Formation of the axial relief at the very slow spreading Southwest Indian Ridge (49 degrees to 69 degrees E), J. Geophys. Res. 104 (1999) 22825–22843.
[69] J.J. Mahoney, J.H. Natland, W.M. White, R. Poreda, S.H. Bloomer, R.L. Fisher, A.N. Baxter, Isotopic and geochemical provinces of the western Indian Ocean spreading centers, J. Geophys. Res. 94 (1989) 4033–4052.
[70] M. Moreira, M.D. Kurz, Subducted oceanic lithosphere and the origin of the 'himu' basalt helium isotopic signature, Earth Planet. Sci. Lett. 189 (2001) 49–57.
[71] C. DeMets, R.G. Gordon, D. Argus, S. Stein, Current plate motions, Geophys. J. Int. 101 (1990) 425–478.
[72] C. DeMets, R.G. Gordon, D.F. Argus, S. Stein, Effect of recent revisions to the geomagnetic reversal time scale on estimates of current plate motions, Geophys. Res. Lett. 21 (1994) 2191–2194.